

Suzaku Discovery of a Hard X-Ray Tail in the Persistent Spectra from the Magnetar 1E 1547.0–5408 during its 2009 Activity

Teruaki ENOTO,¹ Kazuhiro NAKAZAWA,¹ Kazuo MAKISHIMA,^{1,2}
Yujin E. NAKAGAWA,² Takanori SAKAMOTO,³ Masanori OHNO,⁴ Tadayuki TAKAHASHI,⁴
Yukikatsu TERADA,⁵ Kazutaka YAMAOKA,⁶ Toshio MURAKAMI,⁷ and Hiromitsu TAKAHASHI⁸

¹ *Department of Physics, University of Tokyo, 7-3-1 Hongo, Bunkyo-ku, Tokyo, 113-0033*
enoto@junio.phys.s.u-tokyo.ac.jp

² *Cosmic Radiation Laboratory, Institute of Physical and Chemical Research,
Wako, Saitama, 351-0198*

³ *GoddardSpaceFlight Center, NASA, Greenbelt, Maryland, 20771, USA*

⁴ *Department of High Energy Astrophysics, Institute of Space and Astronautical Science,
Japan Aerospace Exploration Agency, 3-1-1 Yoshinodai, Sagami-hara, Kanagawa 229-8510*

⁵ *Department of Physics, Saitama University, 255 Shimo-Okubo, Sakura, Saitama 338-8570*

⁶ *Department of Physics and Mathematics, Aoyama Gakuin University,
5-10-1 Fuchinobe, Sagami-hara, Kanagawa 229-8558, Japan*

⁷ *Department of Physics, Kanazawa University, Kakuma, Kanazawa, Ishikawa 920-1192*

⁸ *Department of Physical Science, Hiroshima University,
1-3-1 Kagamiyama, Higashi-Hiroshima, Hiroshima 739-8526*

(Received ; accepted)

Abstract

The fastest-rotating magnetar 1E 1547.0–5408 was observed in broad-band X-rays with Suzaku for 33 ks on 2009 January 28–29, 7 days after the onset of its latest bursting activity. After removing burst events, the absorption-uncorrected 2–10 keV flux of the persistent emission was measured with the XIS as 5.7×10^{-11} ergs cm⁻² s⁻¹, which is 1–2 orders of magnitude higher than was measured in 2006 and 2007 when the source was less active. The persistent emission was also detected significantly with the HXD in > 10 keV up to at least ~ 110 keV, with an even higher flux of 1.3×10^{-10} ergs cm⁻² s⁻¹ in 20–100 keV. The pulsation was detected at least up to 70 keV at a period of 2.072135 ± 0.00005 s, with a deeper modulation than was measured in a fainter state. The phase-averaged 0.7–114 keV spectrum was reproduced by an absorbed blackbody emission with a temperature of 0.65 ± 0.02 keV, plus a hard power-law with a photon index of ~ 1.5 . At a distance of 9 kpc, the bolometric luminosity of the blackbody and the 2–100 keV luminosity of the hard power-law are estimated as $(6.2 \pm 1.2) \times 10^{35}$ ergs s⁻¹ and 1.9×10^{36} ergs s⁻¹, respectively, while the blackbody radius becomes ~ 5 km. Although the source had not been detected significantly in hard X-rays during the past fainter states, a comparison of the present and past spectra in energies below 10 keV suggests that the hard component is more enhanced than the soft X-ray component during the persistent activity.

Key words: individual (1E 1547.0–5408) — stars: magnetic fields — X-rays: stars

1. Introduction

Luminous neutron stars can be classified into three categories from their dominant energy sources; i.e., rotation-powered, accretion-powered, and magnetic-powered objects. The 1st and 2nd groups are represented by radio pulsars and mass-accreting neutrons-star binaries, respectively. The last category comprises those objects which are called magnetars (Duncan & Thompson 1992; Thompson & Duncan 1995; Thompson & Duncan 1996), mainly observed in X-rays. Magnetars have rotation periods of $P = 2 - 12$ s and period derivatives of $\dot{P} \sim 10^{-11}$ s s⁻¹ (Woods & Thompson 2006; Mereghetti 2008). Their slow rotations cannot afford their high soft

X-ray luminosities, $\sim 10^{35}$ ergs s⁻¹; nor are they accretion-powered objects since they lack evidence of companion stars (e.g., Koyama et al. 1989). Further considering their bursting activity and strong surface magnetic fields ($> 4.4 \times 10^{13}$ G) evaluated from their P and \dot{P} values, the energy source of magnetars is considered to be their strong magnetic fields. Their X-ray luminosities, which generally exceed their spin-down energy losses, can be explained by assuming that their magnetic energies are released faster than their rotational energies.

Currently, ~ 5 Soft Gamma-ray Repeaters (SGR) and ~ 10 Anomalous X-ray Pulsars (AXP) are known as mag-

netars¹. The former objects sometimes emit giant flares with peak luminosities up to $\sim 10^{46}$ ergs s⁻¹, while the latter were discovered by their bright soft X-ray ($\lesssim 10$ keV) emission with luminosities of $(0.1-1) \times 10^{35}$ ergs s⁻¹. Recent studies suggest that SGRs and AXPs are essentially the same class of objects, and their distinction is not fundamental (Mereghetti et al. 2009b); i.e., these names reflect mainly their ways of discovery.

One distinguishing property of magnetars, observed not only from SGRs (Israel et al. 2008; Enoto et al. 2009) but also from AXPs (Gavriil et al. 2002; Kaspi et al. 2003), is occasional periods of high activity wherein numerous “bursts” are emitted. These bursts individually have a typical duration of a few hundred milliseconds and an energy release of $\gtrsim 10^{37}$ ergs. They are thought to represent sudden release of the magnetic energy, leading to the production of hot plasmas and/or energetic particles somewhere in the system.

Bright persistent soft X-rays have long been observed from magnetars in energies below ~ 10 keV. Empirically, these spectra have been fitted by a two-blackbody model or a blackbody (of temperature $kT \sim 0.3-0.6$ keV) plus a soft power-law (of photon index $\Gamma = 2-4$) model, where the power-law is thought to arise via some sort of Compton process (Thompson et al. 2002; Rea et al. 2009).

Recently, INTEGRAL discovered from several magnetars a new emission component (Kuiper et al. 2004; Kuiper et al. 2006; Götz et al. 2006). Becoming prominent in energies above ~ 10 keV, this component exhibits a high pulsed fraction (sometimes $\sim 100\%$ at ~ 100 keV) and extends to ~ 100 keV or more with a surprisingly hard photon index of $\Gamma \sim 1$. Although this discovery aroused wide interest, the origin of this hard X-ray component is still an open question (e.g., Heyl & Hernquist 2005; Beloborodov & Thompson 2007; Baring & Harding 2007).

So far, the hard tail has been detected from three SGRs (SGR 1900+14, SGR 1806-20, and SGR 0501+4516; e.g., Götz et al. 2006; Esposito et al. 2007; Rea et al. 2009) and three AXPs (4U 0142+61, 1RXS J170849.0-400910, and 1E 1841-045; e.g., Kuiper et al. 2004; Kuiper et al. 2006). While some detections from SGRs were made in their burst-active states, those from AXPs are limited to their quiescence. It is hence unknown how the hard tails of AXPs behave in their active periods. When attempting to answer these questions, Suzaku (Mitsuda et al. 2007) provides a great advantage, because it allows us to simultaneously detect the two spectral components of these objects in rather short exposures.

The X-ray source 1E 1547.0–5408 was discovered by the Einstein Observatory in 1980 (Lamb & Markert 1981), and was suggested by recent X-ray observations as a magnetar candidate associated with a young supernova remnant G327.24-0.13 (Gelfand & Gaensler 2007). Subsequent radio observations discovered pulsations with $P = 2.069$ s and $\dot{P} = (2.318 \pm 0.005) \times 10^{-11}$. This established 1E 1547.0–5408 as the fastest rotating magnetar known to date, with a surface field strength of 2.2×10^{14}

G, a characteristic age of 1.4 kyr, and a spin-down luminosity of 1.0×10^{35} ergs s⁻¹, all estimated from the measured P and \dot{P} (Camilo et al. 2007). The radio observation also gave a distance estimate as 9 kpc from its dispersion measure, and identified 1E 1547.0–5408 (PSR J1550-5418) as a second example of transient radio magnetars after XTE J1810-197 (Camilo et al. 2006). Since then, X-ray monitoring observations detected a possible X-ray outburst in 2007 (Halpern et al. 2008). The X-ray pulsation, which was not confirmed in quiescence (Gelfand & Gaensler 2007), was first detected with XMM-Newton during this enhanced activity (Halpern et al. 2008).

Following a possible precursor phase in 2008 October (Krimm et al. 2008a; Krimm et al. 2008b), the Swift Burst Alert Telescope detected bursting activity from 1E 1547.0–5408 on 2009 January 22 (Gronwall et al. 2009). A large numbers of short bursts were recorded by several X-ray satellites, including INTEGRAL (Savchenko et al. 2009; Mereghetti et al. 2009a), Fermi (Connaughton & Briggs 2009), Konus-Wind (Golenetskii et al. 2009), and RHESSI (Bellm et al. 2009). The Wide-band All-sky Monitor (WAM) on board Suzaku also recorded ~ 250 short bursts on January 22 (Terada et al. 2009). Based on this information, a Suzaku Target-of-Opportunity (ToO) observation was conducted on January 28. In the present paper, we report on the result of this observation, focussing on wide-band spectra of the persistent emission. Analysis of short bursts will be reported elsewhere.

2. Observation

The present ToO observation of 1E 1547.0–5408 was carried out with Suzaku from 2009 January 28 21:34 (UT), until January 29 21:32 (UT), with a gross duration of ~ 86 ks. This was 7 days after the onset of its latest strong bursting activity on January 22 (Gronwall et al. 2009). The Suzaku observation partially overlapped with those by INTEGRAL, RXTE, Swift, and Chandra.

Of the three operating cameras of the X-ray Imaging Spectrometer (XIS; Koyama et al. 2007), XIS1 (a back-illuminated or BI CCD) and XIS3 (a front-illuminated or FI CCD) were operated incorporating 1/4 window option to ensure a time resolution of 2 s. Burst option was also employed to avoid possible photon pile-up problems, with its exposure reduced to 1/4 (i.e., 0.5 s exposure and 1.5 s artificial dead-time), although the actual persistent flux of 1E 15470-5408 was low enough to allow an operation without this option. The other one, XIS0, was operated in the timing mode (P-sum mode), which provides a ~ 7.8 ms time resolution, together with only 1-dimensionally projected position information.

The Hard X-ray Detector (HXD; Takahashi et al. 2007) was operated in the standard mode, wherein individual events are recorded with a time resolution of 61 μ s. The target was placed at the “HXD nominal” position.

¹ <http://www.physics.mcgill.ca/pulsar/magnetar/main.html>

3. Data Reduction

Using version 6.6.2 HEADAS software, we analyzed the Suzaku data of 1E 1547.0-5408 (OBSID = 903006010) prepared through version 2.3.12.5 processing. Events were discarded if they were acquired in the South Atlantic Anomaly (SAA) or in regions of low cutoff rigidity (≤ 6 GV for the XIS and ≤ 8 GV for the HXD), or with low Earth elevation angles ($ELV < 5$). The net exposures were 42.6 ks, 10.6 ks, 10.7 ks, and 33.5 ks for XIS0, XIS1, XIS3, and the HXD, respectively. The reduced exposures of XIS1 and XIS3 are due to the burst option (section 2).

3.1. XIS data reduction

For our spectroscopic studies, we use the data from XIS1 and XIS3, which were acquired in the normal imaging mode. The source was detected clearly in the XIS images. On-source XIS1 and XIS3 events were extracted from a region of $2'$ in radius, centered on the source centroid. Background events were derived from a similar region as far away from the source as possible. After subtracting this background, we detected 1E 1547.0–5408 at a burst-inclusive 2–10 keV average count rate as given in table 1. The higher XIS3 rate is due to a relatively hard spectrum and a strong absorption (subsection 4.2), coupled with a more hard-band enhanced efficiency of FI CCDs than that of a BI chip.

The data from XIS0, taken in the timing mode, are used in our timing analyses. We applied some additional corrections to the XIS0 data. Namely, we further filtered the cleaned event file using a selection criteria as $((\text{GRADE}=0) \mid (\text{GRADE}=1) \mid (\text{GRADE}=2))$, and eliminated hot pixels and flickering pixels. In addition, we shifted nominal time assignments of the XIS0 events by -60 ms (i.e., $\text{TIME}-0.06$ s), to take into account the following two effects. One is the read-out time lag when a target is placed at the HXD nominal position (Koyama et al. 2007). The other is a 30 ± 16 ms offset of the absolute timing of the XIS data acquired in the P-sum mode (Matsuda et al., 2009). This offset was measured by observing the Crab pulsar and Her X-1, and comparing the results with simultaneous HXD data of which the relative and absolute timing accuracies had already been verified (Terada et al. 2008). These observations of the two pulsars also confirmed the relative timing accuracy of the XIS.

3.2. HXD-PIN data reduction

From the HXD-PIN data, we subtracted estimated non X-ray background (NXB), which were produced by the “tuned” (LCFITDT) NXB model (Fukazawa et al. 2009). In order to assess the accuracy of the background modeling, we compared its prediction with Earth-occulted portion of the data with 14 ks exposure, because these data are considered to consist solely of the NXB. These two spectra are compared in figure 1. On average, the simulated background was found to fall below the actual Earth occultation data by 2.3% in the 15–70 keV range. The discrepancy is relatively large (13.0%) in the 40–50 keV range, presumably because this band is affected by instru-

mental Gd-K lines (43.0 keV, 42.3 keV, 48.6 keV, and 50 keV). However, if the 40–50 keV range is ignored, the data vs. model difference reduces to only 1.0%. Therefore, we consider the HXD-PIN NXB modeling to be appropriate, and assign it a systematic error of 2.0% after Fukazawa et al. (2009).

From the HXD-PIN data, we also subtracted an expected contribution from the Cosmic X-ray Background (CXB). This was calculated using a recent result from Moretti et al. (2009), which describes the CXB photon number spectrum as

$$\frac{C \cdot \Omega}{(E/E_0)^{\Gamma_1} + (E/E_0)^{\Gamma_2}} \text{ photons s}^{-1} \text{ cm}^{-2} \text{ keV}^{-1} .$$

Here, $C = 1.33 \times 10^{-4}$ is a normalization, $E_0 = 29$ keV is a characteristic energy, $\Gamma_1 = 1.40$ and $\Gamma_2 = 2.88$ are photon indices, and $\Omega = 1.2 \times 10^{-3}$ str is the solid angle of an assumed $2^\circ \times 2^\circ$ emission region with uniform brightness, corresponding to the HXD-PIN “flat” response. The CXB counts are subject to $\sim 11\%$ sky-to-sky fluctuations (Fukazawa et al. 2009). The average CXB flux corresponds to $\sim 5\%$ of PIN-NXB.

Since 1E 1547.0–5408 is located on the Galactic plane at Galactic coordinates of $(l, b) = (-32^\circ.8, -0^\circ.1)$, Galactic Ridge X-ray Emission (GRXE) may contaminate as well. INTEGRAL mapping observations showed that the typical 17–60 keV GRXE flux is less than 1×10^{-9} erg $\text{s}^{-1} \text{ cm}^{-2}$ with an IBIS FOV, on the Galactic disk at $|l| > 20^\circ$ (figure 13 of Krivonos et al. 2007). Within the HXD-PIN FOV, we then expect a flux of $\lesssim 2 \times 10^{-11}$ erg $\text{s}^{-1} \text{ cm}^{-2}$, which is less than $\sim 1\%$ of NXB or $\sim 20\%$ of CXB. This estimate is also supported by a near-by blank sky observation (OBSID = 501043010) at $(l, b) = (-29^\circ.6, -0^\circ.38)$, $3^\circ.2$ off 1E 1547.0–5408: after subtracting the nominal NXB and CXB, the GRXE contribution in the 12–70 keV band was $\sim 30\%$ of the average CXB. Therefore, the GRXE contribution in the HXD-PIN data is negligible.

As summarized in table 1, we were left with positive signals of $\sim 0.174 \pm 0.004$ cts s^{-1} in the 15–70 keV HXD-PIN band, when the NXB and CXB were both subtracted. Thus, the signal detection is highly significant in the HXD-PIN data, because the systematic error (2.0%) is estimated to be $\sim 7 \times 10^{-3}$ cts s^{-1} in the same band.

3.3. HXD-GSO data reduction

The simulated background of HXD-GSO, also produced by the “tuned” model, was evaluated again by the Earth-occulted data. As shown in figure 1, the simulated background systematically under-predicted the actual Earth occulted HXD-GSO data by 0.53% and 1.4% in the 50–114 and 115–578 keV band, respectively. Conservatively, we hence subtracted the HXD-GSO background after increasing it by 0.53% and 1.4% over the above ranges, respectively, and assigned systematic uncertainties of 0.60% and 0.59% therein (Fukazawa et al. 2009).

After subtracting the NXB and considering the above systematic errors, the HXD-GSO signal count rate became as shown in table 1. Therefore, the signal has an

overall significance of $\sim 2.3\sigma$ in the 50–114 keV range, but is insignificant in higher energies.

3.4. Elimination of burst events

Figure 2 shows a dead-time corrected and background-subtracted XIS1+XIS3 light curve in the 2–10 keV range. There, a number of short burst events can be noticed as sharp spikes. By visually inspecting this XIS1+XIS3 light curve and that of HXD-PIN (15–70 keV), produced with a bin width of 2 s (one frame) and 1 s, respectively, we identified 13 prominent burst candidates. Some of them were detected by both instruments, while the others by either of them. Then, the XIS and HXD data acquired within 3-s time intervals both before and after each of these bursts were discarded.

After this burst elimination, the background-subtracted average count rates of XIS, XIS3, and HXD-PIN became as given in table 1. Although the remaining data must still contain smaller bursts, their summed contribution is estimated to be no more than 0.1%.

3.5. Contaminating sources

During the Suzaku observation, the 10–30 keV HXD-PIN signal intensity, after subtracting the NXB and CXB, was ~ 10 mCrab. According to the INTEGRAL General Reference Catalog (`gnrl_refr_cat_0030.fits`), the HXD-PIN full FOV ($\sim 34' \times \sim 34'$) contained 4 contaminating source candidates detected with ASCA (Sugizaki et al. 2001). Their 10–30 keV intensities (using JEM-X), 0.01 mCrab of AX J1550.5-5408, 0.26 mCrab of AX J1549.8-5416, 0.01 mCrab of AX J1553.5-5347, and 0.41 mCrab of AX J1549.0-5420, sum up to $< 10\%$ of the signal from the 1E 1547.0–5408 field. Although these may be variable X-ray sources, AX J1550.5-5408 was not detected neither with the XIS, nor in a 3–10 keV Swift/XRT image obtained on 2009 January 29. The Swift/XRT count rate of AX J1549.8-5416 was $\lesssim 0.01$ times that of 1E 1547.0-5408 on the same occasion. In addition, AX J1553.5-5347 and AX J1549.0-5420 were located outside the FWHM FOV of HXD-PIN, with their aperture transmissions of $\lesssim 10\%$ and $\lesssim 50\%$, respectively. Further considering lack of reports on X-ray brightening from none of these sources, we regard their contamination as negligible. This assumption is further confirmed in section 4.2.

As summarized in table 2, the $4^\circ \times 4^\circ$ HXD-GSO FOV (and outside that of HXD-PIN) contains 5 sources with 20–60 keV intensities of > 3 mCrab. Since they are also variable X-ray sources, we examined the RXTE/ASM quick-look data (Jahoda et al. 1996) for their intensities over 10 days around our Suzaku observation. All of them were found, during this period, to be < 20 mCrab in the 2–10 keV range. When we assume spectral shapes from the INTEGRAL General Reference Catalog and normalizations of the ASM monitoring, their 50–200 keV intensities are estimated to be less than $\sim 0.01\%$ level of the HXD-GSO NXB. Therefore we can also ignore source confusion within the HXD-GSO FOV. From these examinations, we regard the burst-removed signals detected with HXD-GSO (below 114 keV), given in the last column of table 1, as

coming also from 1E 1547.0–5408 itself.

4. Data Analysis and Result

4.1. Pulsation

After eliminating the 13 burst candidates, all the XIS0 and HXD event arrival times were converted to those measured at the solar system barycenter, using a source position of $(\alpha, \delta)_{2000} = (15^{\text{h}}50^{\text{m}}54.11^{\text{s}}, -54^\circ 18' 23.7'')$ as well as the spacecraft orbital information. Then, via standard epoch-folding technique, we searched the 2–10 keV XIS P-sum data and the 12–70 keV background-inclusive HXD-PIN data for the known 2.0 s X-ray period (Halpern et al. 2008). The analysis was performed over a trial period range of 2.0713–2.0730 s, with a step of 4×10^{-6} s which corresponds to a change of 0.08 cycle across the overall time span of ~ 86 ks. The derived periodograms are shown in figure 3. A significant ($\chi^2/\nu = 41.8/12$ for the HXD-PIN data, and $\chi^2/\nu = 141.1/14$ for the XIS P-sum data) periodicity was found at a consistent period of

$$P = 2.072135 \pm 0.00005 \text{ s} \quad (1)$$

as of epoch 54859 (MJD). The analysis employed a period derivate $\dot{P} = 2.35 \times 10^{-11} \text{ s s}^{-1}$, from multi-satellite timing observations of 1E 1547.0–5408 (Israel et al. private communication) which covers our Suzaku observation epoch. We use equation (1) and $\dot{P} = 2.35 \times 10^{-11} \text{ s s}^{-1}$ for our subsequent timing analyses.

Figure 4 shows energy-sorted pulse profiles derived from XIS0, HXD-PIN, and HXD-GSO, folded at equation (1). The null hypothesis probability of the pulse detection is $< 1 \times 10^{-4}$, $< 1 \times 10^{-4}$, 3×10^{-4} , 0.06, and 0.47, in the 1–3 keV (XIS0), 3–10 keV (XIS0), 10–25 keV (HXD-PIN), 25–70 keV (HXD-PIN), and 50–114 keV (HXD-GSO) energy bands, respectively. Therefore, the pulsations are significant in the XIS and the low-energy ($\lesssim 25$ keV) HXD-PIN data with > 3 sigma, although inconclusive in the high-energy HXD-PIN band and insignificant in the HXD-GSO data. The HXD-PIN data were further analyzed with the Z-squared tests (Buccheri et al. 1983; Brazier 1994). Then, the 10–25 keV and 25–70 keV HXD-PIN data yielded $Z_2^2 = 19.7$ (the total event number being $N \simeq 1.7 \times 10^4$) and 12.7 ($N \simeq 6.5 \times 10^4$), which correspond to null hypothesis probabilities of 6×10^{-4} and 0.013, respectively. In other words, the high-energy (25–70 keV) HXD-PIN data are modulated, with a $\sim 99\%$ confidence, at the same period as the lower-energy photons, even though the χ^2 significance is not high enough. Therefore, we discuss the 25–70 keV pulse profile as well.

As shown by figure 4 and reported before (Halpern et al. 2008), the pulse profiles of this object are relatively shallow. The peak-to-peak pulsed fractions, defined as $(F_{\text{max}} - F_{\text{min}})/(F_{\text{max}} + F_{\text{min}})$, are presented in figure 5 as a function of the photon energy. Here, F_{max} and F_{min} are the maximum and minimum background-subtracted count rates across the pulse phase, respectively. Error bars include Poisson fluctuations and the systematic uncertainties of the NXB. Although the pulsed fraction tends to increase towards higher energies as observed in some

magnetars (Kuiper et al. 2006), the dependence is insignificant when considering the errors.

4.2. Persistent phase-averaged spectrum

Figure 6a shows time-averaged and dead-time-corrected spectra of the persistent emission from 1E 1547.0–5408, derived over a broad energy band with XIS1, XIS3, HXD-PIN, and HXD-GSO. The data accumulation and background subtraction were carried out as described in sections 3.1, sections 3.2, and sections 3.3. The 13 burst events were excluded (section 3.4). In addition, as described in sections 3.3, the 0.6% systematic errors were assigned to the HXD-GSO data, while the 2.0% systematic error in the HXD-PIN NXB (subsection 3.2) is separately considered later. In agreement with figure 4e and the results in sections 3.3, the hard X-ray signals were detected with HXD-GSO at least up to 114 keV with 2.3 sigma level. This significance increases to $>3\sigma$ when the upper bound energy is lowered to 70 keV of HXD-PIN.

Since the small pulsed fractions (figure 5) and the short exposure (33 ks with the HXD) make it difficult to perform detailed phase-resolved spectroscopy, hereafter we analyze only these phase-averaged spectra. The analysis utilized `xspec` version 12.5, with the HXD response matrices version 2009-04-03, and the XIS response matrices created using `xissimarfgen` and `xisrmfgen`.

As clearly revealed by figure 6c in an νF_ν spectral form, the detected HXD-PIN and HXD-GSO signals show a prominent hard component above 10 keV, just like in some other magnetars (e.g., Kuiper et al. 2006). This provides the first detection of such a hard spectral component from this magnetar. In deriving figure 6c, the cross-normalization factor of HXD-PIN relative to the XIS was fixed at 1.181 after Maeda et al (2008). Since the XIS and the HXD-PIN spectra thus connect smoothly to each other, the HXD-PIN signals are unlikely to be contaminated by other sources that are inside the HXD-PIN FOV but outside that of the XIS. Any signal from such contaminants is estimated to be $\lesssim 24\%$ at 15 keV of the HXD-PIN spectrum. This level would be much lower in harder energies, considering that such sources, most likely low-mass neutron star binaries (Sugizaki et al. 2001), should exhibit softer spectra than the observed one.

In order to approximately characterize this hard component, we fitted the 15–70 keV HXD-PIN data in figure 6a with a single power-law model. The fit was successful with $\chi^2/\text{d.o.f} = 30.4/31 = 0.98$, and yielded a photon index of $\Gamma = 1.41_{-0.16}^{+0.17}(\text{stat.}) \pm 0.04(\text{sys.})$, and a 15–70 keV flux of $F_x = 1.38_{-0.19}^{+0.21}(\text{stat.}) \pm 0.09(\text{sys.}) \times 10^{-10} \text{ ergs s}^{-1} \text{ cm}^{-2}$. Here, the systematic errors were estimated by increasing or decreasing the PIN-NXB by 2% (subsection 3.2). The result implies that the hard component is rather featureless.

As a next step, we included the XIS1, XIS3, and HXD-GSO spectra. The absorbing column density N_{H} was allowed to vary. Then, as shown in figure 6 and table 3a, the entire 0.7–114 keV spectra were successfully fitted by adding a blackbody with a temperature $kT = 0.65$ keV to the flat power-law which was found with the HXD-PIN

data. Hereafter, we call this “blackbody+powerlaw” modeling Model A. While the errors in table 1 are statistical only, inclusion of the HXD-PIN systematic errors affected Γ by ± 0.02 , and the 20–100 keV flux by $\pm 8\%$. The fit is reproduced in figure 6c in an νF_ν form.

Although this Model A gave an acceptable result, we tried to replace the blackbody component, accounting for the soft signals, with a Comptonized blackbody model. This is because a soft power-law tail with $\Gamma=2-4$, suggestive of Comptonization, often emerges in the soft X-ray (< 10 keV) spectra of magnetars (Mereghetti 2008). In order to take into account this effect, we constructed a simple formalism of the Comptonized blackbody radiation model (Rybicki & Lightman 1979; Tiengo et al. 2005; Halpern et al. 2008), which is described in detail in Appendix. In high energies this model approaches a power-law form with a steep photon index Γ_{comp} , but it is free from an infrared divergence that plagues a more conventional modeling of a blackbody plus a steep power-law. As presented in figure 7 (left) and table 3, this Comptonized blackbody plus hard power-law model, hereafter called Model B, also gave an acceptable (and slightly better) fit to the data. The photon index of the soft tail was obtained as $\Gamma_{\text{comp}} \sim 4.9$ (table 3); that of the hard power-law remained unchanged from that of Model A within errors; and the blackbody temperature decreased to $kT = 0.48$ keV.

Alternatively, to represent the above soft power-law component, we may also employ 1D semi-analytical resonant Compton scattering model after (Rea et al. 2009) using `xspec12` local model “RCS.mod”. This local model assumes repeated resonant cyclotron scatterings of the thermal radiation from the surface by hot electrons in the neutron star magnetosphere. The model, hereafter Model C, also gave an acceptable fit (figure 7 right), although it requires a large optical depth (table 3).

The hard-tail slope, $\Gamma \sim 1.5$, must steepen at some energies, in order for the hard-component luminosity not to diverge. To obtain a constraint on such a high-energy steepening, we employed Model A, and multiplied its hard power-law with an exponential cutoff factor of the form $\exp(-E/E_{\text{cut}})$, where E is the photon energy and E_{cut} is a parameter. Then, the data gave a constraint as $E_{\text{cut}} > 200$ keV at the 90%-confidence limit.

5. Discussion

5.1. Broad-band information

The present Suzaku ToO observation of 1E 1547.0–5408, made 7 days after the onset of the 2009 January bursting activity, have allowed the first study of this fastest-rotating magnetar over an extremely broad band spanning two orders of magnitude in energy. The most important finding is the first discovery from this source of the very hard component, which was so far observed from some (though not all) other magnetars. This component dominates the burst-removed persistent emission spectra of 1E 1547.0–5408 in $\gtrsim 7$ keV, and extends at least up to ~ 100 keV with $\Gamma \sim 1.5$ without

evidence of prominent spectral features or steepening ($E_{\text{cut}} > 200$ keV).

We discovered that the hard X-rays are pulsed at the same period as the soft X-rays, although the pulsed fractions are considerably smaller (figure 5) than those of typical magnetars.

As summarized in table 3, the measured 20–100 keV flux (1.3×10^{-10} erg s $^{-1}$ cm $^{-2}$) exceeds the unabsorbed 2–10 keV flux (8.0×10^{-11} erg s $^{-1}$ cm $^{-2}$) by a factor of $R = 1.57 \pm 0.15$. (This factor becomes 2.1 if instead using the absorption-uncorrected 2–10 keV flux in table 3.) Therefore, at least during this active period, the emission appeared mainly in hard X-ray energies. If we separate the soft and hard components referring to Model A for simplicity, and employ a distance $d = 9$ kpc as a fiducial value, the absorption-corrected bolometric luminosity of the soft component (blackbody) becomes $L_{\text{BB}} = (6.2 \pm 1.2) \times 10^{35} (d/9 \text{ kpc})^2$ ergs s $^{-1}$, whereas that of the hard component in the 2–100 keV band becomes $1.9 \times 10^{36} (d/9 \text{ kpc})^2$ ergs s $^{-1}$.

Enoto et al. (2010) pointed out that the 20–100 keV to 2–10 keV flux ratio R of magnetars, as introduced above, negatively correlates with their characteristic age τ_c . During the present activity, 1E 1547.0–5408 exhibited $R = 1.57$ as derived above. This ratio is higher than those of magnetars with older characteristic ages (typically AXPs; e.g., $R \sim 0.7$ for 4U 0142+61 with $\tau_c = 70$ kyr), while lower than those of objects with younger characteristic ages (typically SGRs; e.g. $R \sim 2.8$ for SGR 1806–20 with $\tau_c = 0.2$ kyr). Furthermore, the hard-tail slope of 1E 1547.0–5408 ($\Gamma \sim 1.5$) is in between those of typical AXPs ($\Gamma \sim 1.0$) and of typical SGRs ($\Gamma = 1.8 - 3.1$; Götz et al. 2006). This is reinforced when we plot the photon index of 1E 1547.0–5408 on figure 3 of Kaspi & Boydston 2010, which reports a correlation between the hard-band photon index and the magnetic field strength. These properties, together with $\tau_c = 1.4$ kyr, make the activated 1E 1547.0–5408 an object in between the typical SGRs with young characteristic ages and the typical AXPs with older characteristic ages.

5.2. Modeling of the soft component

Taking into account the hard tail component, the broad-band Suzaku spectra have been reproduced successfully by the three alternative modelings (Models A, B, and C) of the soft component. In all cases, the hydrogen column density was obtained as $N_{\text{H}} = (3.2 - 4.0) \times 10^{22}$ cm $^{-2}$ (table 3), which is consistent with the past XMM-Newton and Swift measurements in a much faint state in 2006–2007 (Halpern et al. 2008). Although this N_{H} is 1.5–1.8 times higher than the Galactic HI column density in the direction of 1E 1547.0–5408, 2.2×10^{22} cm $^{-2}$ (Dickey & Lockman 1990), the difference can be explained away by including the H $_2$ gas contribution as judged from CO observations (Halpern et al. 2008).

Although the three models all proved to be successful, Model B and Model C give better chi-squares than Model A (figure 7, table 3). According to F -tests, chance probabilities of the fit improvement from Model A to Model B,

and Model A to Model C, are 1.2×10^{-3} and 8.3×10^{-3} , respectively. Therefore, the hardest end of the soft component is suggested to exhibit a power-law like extension as found in the quiescent spectrum of this object (Halpern et al. 2008), rather than turning over exponentially.

5.3. Effects of the enhanced activity

While 1E 1547.0–5408 showed AXP-like soft X-ray spectra in quiescence (Gelfand & Gaensler 2007; Halpern et al. 2008), its burst properties recorded in the present activity are very similar to those of typical SGRs (Mereghetti et al. 2009). Therefore, this object is considered to exhibit properties typical of both SGRs and AXPs, depending on its activity states. It is hence expected to provide us a unique opportunity in comparing magnetars of different activity levels.

Past Swift and XMM-Newton observations of this object reported a historical minimum 1–8 keV flux (absorption uncorrected) of 3.3×10^{-13} ergs cm $^{-2}$ s $^{-1}$ in 2006 August, while a much enhanced value of 4.6×10^{-12} ergs cm $^{-2}$ s $^{-1}$ during the previous outburst in 2007 January (Halpern et al. 2008). The same quantity measured in the present observation, $(5.2 \pm 0.2) \times 10^{-11}$ ergs cm $^{-2}$ s $^{-1}$ (using Model A for simplicity), is even ~ 158 and ~ 11 times higher than those measured in 2006 August and 2007 January, respectively. These large soft X-ray variations are similar to those of the transient magnetars XTE J1810–197 and CXOU J164710.2–455216 (Halpern et al. 2008).

In evaluating how the activity affected the soft component, let us for simplicity refer to Model A, even though the soft component may not be a pure blackbody (section 5.2). In terms of Model A, we measured a blackbody temperature of 0.65 ± 0.02 keV (table 3), which is ~ 1.5 times higher than the values of $0.43_{-0.04}^{+0.03}$ keV measured in 2006 during quiescence (Gelfand & Gaensler 2007). Likewise, the blackbody radius of $5.2_{-0.3}^{+0.4} (d/9\text{kpc})^2$ km from our Model A (table 3), which implies a sizable fraction of a neutron star surface, is larger than the values of 1.7–3.7 km measured in 2006 August to 2007 August (Gelfand & Gaensler 2007; Halpern et al. 2008). Therefore, the enhanced activity caused increases, both in the area and temperature, of the blackbody source located presumably on the neutron star surface. A qualitatively similar result was obtained by Halpern et al. (2008), utilizing a factor 14 change in the 1–8 keV flux from 2006 August to 2007 June.

Since the present Suzaku observation has allowed the first detection of 1E 1547.0–5408 in energies above ~ 10 keV, it is not trivial to evaluate how the hard tail was enhanced by the bursting activity. Let us then use spectra below 10 keV, and define a fractional luminosity carried by any “non-blackbody” component, as $\eta = (L_{\text{tot}} - L_{\text{BB}})/L_{\text{tot}}$, where L_{tot} is the absorbed 1–10 keV total luminosity at 9 kpc, and L_{BB} is the bolometric luminosity of the soft blackbody. In the present case, we have $L_{\text{BB}} = (6.2 \pm 1.2) \times 10^{35}$ ergs s $^{-1}$ (section 5.1), together with $L_{\text{tot}} = 1.1 \times 10^{36}$ ergs s $^{-1}$, and hence $\eta \sim 0.44$. Thus, even in energies below 10 keV, nearly half the per-

sistent X-ray flux in the present activity is considered to be carried by the hard component, unless it steeply cuts off toward lower energies.

The results by Halpern et al. (2008), obtained in the less active periods in 2006–2007, in contrast imply $\eta = 0.26 - 0.32$. We therefore infer that the hard tail component is more strongly affected by the activity variation than the soft emission. This inference is reinforced if we notice that the “non-blackbody” fraction in 2006–2007 could be at least partially attributed, e.g., to the Comptonization tail of the soft component itself, rather than to the genuine hard tail component. In agreement with this inference, Enoto et al. (2010) suggest that the hard component of SGR 0501+4156 decayed, after its 2008 August emergence, more rapidly than the soft component.

Yet another effect of the enhanced activity is a marked increase in the pulsed fraction. In the less active state in 2007, the pulsed fraction was measured with XMM-Newton to be $\sim 7\%$ (Halpern et al. 2008). This value was defined, differently from our definition (section 4.1), as a fraction of counts above a minimum of the folded pulse profile. Even using this definition, the 1–3 and 3–10 keV pulsed fraction of the present XIS0 data is obtained as $\sim 17\%$ and $\sim 20\%$, respectively, which are not much different from these given in figure 5. Thus, the pulsed fraction in the present active state is 2–3 times higher than that in the less active one. Such a change of the pulse fraction between the outburst and quiescence has been reported also from XTE J1810-197 and CXOU J164710.2-455216 (Israel et al. 2007). A possible scenario is that these objects are observed relatively parallel to their rotational axes, and a blackbody emitter localized on the neutron-star surface (may or may not be at a magnetic pole) is always visible from us normally. As the activity gets higher, the blackbody emitter, gradually increasing in area as we found above, may start to exhibit self-eclipse as the star rotates.

6. Summary

On 2009 January 28–29, we performed a SuzakuToO observation of the fastest-rotating magnetar 1E 1547.0–5408 in its burst-active state.

1. In addition to short bursts, the persistent X-ray emission was detected over a broad energy band, from ~ 0.8 keV at least up to ~ 100 keV. The 20–100 keV flux of 1.3×10^{-10} ergs s $^{-1}$ cm $^{-2}$, measured for the first time from this source, exceeds by a factor of 1.6 (or 2.1) the absorption-corrected (or uncorrected) 2–10 keV flux.
2. The pulsation was detected up to ~ 70 keV at a period of 2.072135 s. Although the pulsed fraction (16–28%) is lower than those of most of other magnetars, it is considerably higher than was observed previously from this object in quiescence.
3. The broad band X-ray spectra were fitted successfully by a soft blackbody of $kT = 0.65$ keV plus an extremely hard power-law component of $\Gamma \sim 1.5$. At

a 9 kpc distance, the bolometric luminosity of the former becomes $(6.2 \pm 1.2) \times 10^{35}$ ergs s $^{-1}$, while the 2–100 keV luminosity of the latter 1.9×10^{36} ergs s $^{-1}$.

4. Compared to the quiescence, the blackbody temperature increased by a factor of ~ 1.5 , and the blackbody radius (~ 5 km at 9 kpc) also increased. As a result, the 2–10 keV flux increased by 1–2 order of magnitude compared to the previous fainter states in 2006 and 2007.
5. Replacing the blackbody with a Comptonized blackbody or an RCS model improved the fit, suggesting that the soft component deviates from a pure blackbody.
6. The hard X-ray flux, though not measured previously, is inferred to have increased during the activity by a larger factor than the soft X-ray flux. In the present data, the hard component still carries nearly half the flux in energies below 10 keV.
7. These results can be understood by considering that 1E 1547.0–5408, during the activity, became a magnetar that has properties in between those of the most active SGRs and of the least active AXPs.

We thank the Suzaku operation team for the successful accomplishment of the present ToO observation, and are grateful to Tadayasu Dotani for his advices on the XIS timing modes. We also thank Nanda Rea and Gianluca Israel for helpful discussions and for providing us with useful information. In §4, we used quick-look results provided through a website by the ASM/RXTE team. TE is supported by the JSPS Research Fellowship for Young Scientists. The present work was supported in part by Grant-in-Aid for Scientific Research (S), No. 18104004.

Appendix. Comptonized blackbody Model

When an X-ray photon with an energy ϵ' is up-scattered in a single Compton process to an energy ϵ , its energy becomes $\epsilon_k \sim \epsilon' A^k$ after k scatterings, where $A \equiv \epsilon/\epsilon'$ denotes an amplification factor. When the scatterer has an optical depth τ and is optically thin, a probability for a photon to experience k scatterings is given as τ^k . These scatterings changes the original photon number flux $I(E')$ to

$$I(E) \sim I(E')\tau^k = I(E') \left(\frac{E}{E'} \right)^{-\alpha},$$

where $\alpha \equiv -\ln\tau/\ln A$. If the original radiation is a blackbody radiation (in photon number flux),

$$I(E') = \frac{E'^2}{\exp(E'/kT) - 1} \text{ photons s}^{-1} \text{ cm}^{-2} \text{ keV}^{-1}$$

with a temperature kT and a normalization factor C , then the modified spectra after multiple scatterings becomes,

$$I(E)dE = \int_0^E I(E') \left(\frac{E}{E'} \right)^{-\alpha} dE' \text{ photons s}^{-1} \text{ cm}^{-2}$$

$$\begin{aligned}
I(E) &= CE^{-1-\alpha} \int_0^E \frac{E'^{2+\alpha}}{\exp(E'/kT) - 1} dE' \\
&= CE^{-\Gamma_{\text{comp}}} \int_0^E \frac{E'^{\Gamma_{\text{comp}}+1}}{\exp(E'/kT) - 1} dE'.
\end{aligned}$$

Here a photon index in the high energy range is defined as $\Gamma_{\text{comp}} = 1 + \alpha$, because it has a form of $I(E) \propto E^{-(1+\alpha)} = E^{-\Gamma_{\text{comp}}}$ at $E/kT \gg 1$. This also has the Reyleigh-Jean form in low energy region ($E/kT \ll 1$), $I(E) \propto E$ photons $\text{s}^{-1} \text{cm}^{-2} \text{keV}^{-1}$. We implemented this integration in `xspec12` with the GNU Scientific Library (GSL) codes, where the integration has a relative accuracy of 10^{-4} .

References

- Baring, M. G., & Harding, A. K. 2007, *Ap&SS*, 308, 109
- Bellm, E., Smith, D. M., & Hurley, K. 2009, *GRB Coordinates Network*, 8857, 1
- Beloborodov, A. M., & Thompson, C. 2007, *ApJ*, 657, 967
- Brazier, K. T. S. 1994, *MNRAS*, 268, 709
- Buccheri, R., et al. 1983, *A&A*, 128, 245
- Camilo, F., Ransom, S. M., Halpern, J. P., & Reynolds, J. 2007, *ApJL*, 666, L93
- Camilo, F., Ransom, S. M., Halpern, J. P., Reynolds, J., Helfand, D. J., Zimmerman, N., & Sarkissian, J. 2006, *Nature*, 442, 892
- Connaughton, V., & Briggs, M. 2009, *GRB Coordinates Network*, 8835, 1
- Dickey, J. M., & Lockman, F. J. 1990, *ARA&A*, 28, 215
- Duncan, R. C., & Thompson, C. 1992, *ApJL*, 392, L9
- Enoto, T., et al. 2009, *ApJL*, 693, L122
- Enoto, T., et al. 2010, *ApJ*, submitted
- Esposito, P., et al. 2007, *A&A*, 476, 32 1
- Fukazawa, Y., et al. 2009, *arXiv:0901.0419*
- Gavriil, F. P., Kaspi, V. M., & Woods, P. M. 2002, *Nature*, 419, 142
- Gelfand, J. D., & Gaensler, B. M. 2007, *ApJ*, 667, 1111
- Golenetskii, S., et al. 2009, *GRB Coordinates Network*, 8851, 1
- Götz, D., Mereghetti, S., Tiengo, A., & Esposito, P. 2006, *A&A*, 449, L31
- Gronwall, C., Holland, S. T., Markwardt, C. B., Palmer, D. M., Stamatikos, M., & Vetere, L. 2009, *GRB Coordinates Network*, 8833, 1
- Halpern, J. P., Gotthelf, E. V., Reynolds, J., Ransom, S. M., & Camilo, F. 2008, *ApJ*, 676, 1178
- Heyl, J. S., & Hernquist, L. 2005, *MNRAS*, 362, 777
- Israel, G. L., Campana, S., Dall’Osso, S., Munro, M. P., Cummings, J., Perna, R., & Stella, L. 2007, *ApJ*, 664, 448
- Israel, G. L., et al. 2008, *ApJ*, 685, 1114
- Jahoda, K., Swank, J. H., Giles, A. B., Stark, M. J., Strohmayer, T., Zhang, W., & Morgan, E. H. 1996, *Proc. SPIE*, 2808, 59
- Kaspi, V. M., Gavriil, F. P., Woods, P. M., Jensen, J. B., Roberts, M. S. E., & Chakrabarty, D. 2003, *ApJL*, 588, L93
- Kaspi, V. M., & Boydston, K. 2010, *ApJL*, 710, L115
- Koyama, K. et al. 1989, *PASJ*, 41, 461
- Koyama, K. et al. 2007, *PASJ*, 59, S23
- Krimm, H. A. et al. 2008a, *GRB Coordinates Network*, 8311, 1
- Krimm, H. A. et al. 2008b, *GRB Coordinates Network*, 8312, 1
- Krivonos, R., Revnivtsev, M., Churazov, E., Sazonov, S., Grebenev, S., & Sunyaev, R. 2007, *A&A*, 463, 957
- Kuiper, L., Hermsen, W., & Mendez, M. 2004, *ApJ*, 613, 1173
- Kuiper, L., Hermsen, W., den Hartog, P. R., & Collmar, W. 2006, *ApJ*, 645, 556
- Lamb, R. C., & Markert, T. H. 1981, *ApJ*, 244, 94
- Mereghetti, S. 2008, *A&A Rev.*, 15, 225
- Mereghetti, S., Gotz, D., von Kienlin, A., Beckmann, V., Savchenko, V., Neronov, A., Beck, M., & Borkowski, J. 2009a, *GRB Coordinates Network*, 8841, 1
- Mereghetti, S., et al. 2009b, *ApJL*, 696, L74
- Matsuta, K., Dotani, T., Ozaki, M., Bamba, A., Tsujimoto, M., Tsuru, T., G., Matsumoto, H., Hayashida, K., Tsunemi, H., and the XIS team, 2009, *Suzaku Conference “The Energetic Cosmos: from Suzaku to ASTRO-H”*, Proceeding (in press)
- Mitsuda, K., et al. 2007, *PASJ*, 59, 1
- Moretti, A., et al. 2009, *A&A*, 493, 501
- Rybicki, G. B., & Lightman, A. P. 1979, *New York, Wiley-Interscience*, 1979. 393 p.,
- Rea, N., et al. 2009, *MNRAS*, 396, 2419
- Savchenko, V., et al. 2009, *GRB Coordinates Network*, 8837, 1
- Sugizaki, M., Mitsuda, K., Kaneda, H., Matsuzaki, K., Yamauchi, S., & Koyama, K. 2001, *ApJS*, 134, 77
- Takahashi, T. et al. 2007, *PASJ*, 59, S35
- Terada, Y., et al. 2008, *PASJ*, 60, S25
- Terada, Y., et al. 2009, *GRB Coordinates Network*, 8845, 1
- Thompson, C., & Duncan, R. C. 1995, *MNRAS*, 275, 255
- Thompson, C., & Duncan, R. C. 1996, *ApJ*, 473, 322
- Thompson, C., Lyutikov, M., & Kulkarni, S. R. 2002, *ApJ*, 574, 332
- Tiengo, A., Mereghetti, S., Turolla, R., Zane, S., Rea, N., Stella, L., & Israel, G. L. 2005, *A&A*, 437, 997
- Woods, P. M., & Thompson, C. 2006, *Compact stellar X-ray sources*, 547

Table 1. Count rates from individual detectors.

Detector	Energy (keV)	Background-inclusive	Background-subtracted	Burst-removed
XIS1*	2–10	1.44±0.01	1.40±0.01	1.34±0.01
XIS3*	2–10	1.64±0.01	1.61±0.01	1.53±0.01
HXD-PIN*	15–70	0.528±0.004	0.174±0.004	0.168±0.004
HXD-GSO†	50–114	9.40±0.06	0.151±0.064	0.148±0.064
HXD-GSO†	114–578	27.01±0.19	0.030±0.192	0.028±0.192

*: Counts s^{-1} with statistical 1σ errors.

†: Counts s^{-1} , with statistical (1σ) and systematic errors.

Table 2. Contaminating source candidates*

Name	Type	Intensity [†]	Flux [‡]
1H 1538-522	HMXB	9.8 mCrab	$\sim 1 \times 10^{-5}$
H 1608-522	LMXB	19 mCrab	$\sim 8 \times 10^{-5}$
XTE J1550-564	LMXB	12 mCrab	$\sim 2 \times 10^{-4}$
XTE J1543-568	HMXB	0.23 mCrab	$\sim 4 \times 10^{-4}$
Cir X-1	LMXB	<0.1 mCrab	$< 5 \times 10^{-7}$

*: Source within the FOV of HXD-GSO with >1 mCrab in the 20–60 keV range, from the INTEGRAL General Reference Catalog.

†: Average 2–10 keV intensity, measured by the ASM/RXTE, over 10 days around the Suzaku observation.

‡: Predicted flux (photons $\text{s}^{-1} \text{cm}^{-2}$) of HXD-GSO, using spectral parameters in the INTEGRAL General Reference Catalog, and normalized by the ASM intensities. The angular transmission of the HXD-GSO FOV is not considered.

Table 3. Phase parameters averaged for each spectral model.*

Model	averaged		spec-
	(A)	(B)	model.*
	BB+PL	CBB+PL	RCS+PL
N_{H} (10^{22}cm^{-2})	3.2 ± 0.1	3.3 ± 0.1	$4.0^{+0.4}_{-0.6}$
kT (keV)	0.65 ± 0.02	$0.48^{+0.05}_{-0.04}$	–
R (km) [†]	$5.2^{+0.4}_{-0.3}$	–	–
$\alpha = \Gamma_{\text{comp}} - 1$	–	$3.9^{+1.9}_{-0.8}$	–
RCS T (keV)	–	–	$0.12^{+0.17}_{-0.01}$
RCS τ	–	–	>7
RCS β	–	–	$0.49^{+0.01}_{-0.19}$
Absorbed F_{soft} [‡]	$5.71^{+0.15}_{-0.18}$	$5.68^{+0.45}_{-0.11}$	$5.67^{\text{ND}}_{\text{ND}}$
Unabsorb. F_{soft} [‡]	$7.95^{+0.21}_{-0.25}$	$7.99^{+0.63}_{-0.15}$	$7.98^{\text{ND}}_{\text{ND}}$
Γ_{hard}	$1.54^{+0.06}_{-0.05}$	$1.34^{+0.14}_{-0.15}$	$1.33^{+0.08}_{-0.08}$
F_{hard} #	$12.5^{+0.8}_{-1.1}$	$14.4^{+1.9}_{-1.6}$	$14.7^{+1.3}_{-1.1}$
$\chi^2/\text{d.o.f}$	298.9/278	287.9/277	288.7/276
	= 1.08	= 1.04	= 1.04
Null hyp. prob.	0.19	0.31	0.32

*: BB, PL, CBB, and RCS represent blackbody, power-law, (magnetic) comptonized blackbody, and resonant cyclotron scattering, respectively. ND represents “not determined.” All the quoted errors are only statistical at the 90% confidence level.

†: Blackbody radius assuming a distance of 9 kpc.

‡: 2–10 keV flux in $10^{-11} \text{ergs s}^{-1} \text{cm}^{-2}$.

#: Unabsorbed 20–100 keV flux in $10^{-11} \text{ergs s}^{-1} \text{cm}^{-2}$.

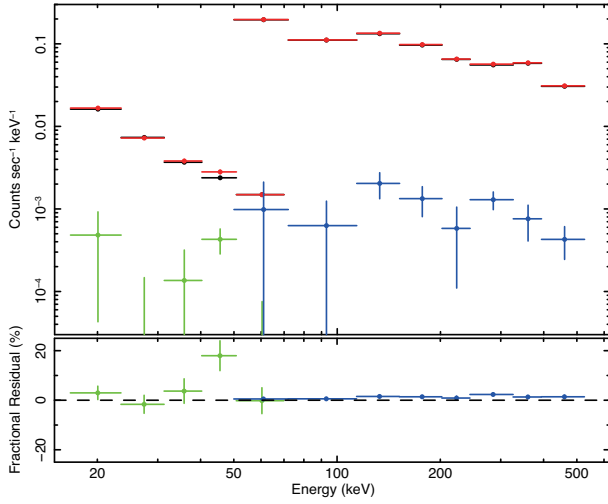


Fig. 1. (Top) A comparison between the Earth occulted HXD-PIN and HXD-GSO data (red) and the corresponding simulated background data (black). The residuals (data minus simulation) are shown in green for HXD-PIN and in blue for HXD-GSO. (Bottom) Fractional residuals, namely (data - simulation) / simulation.

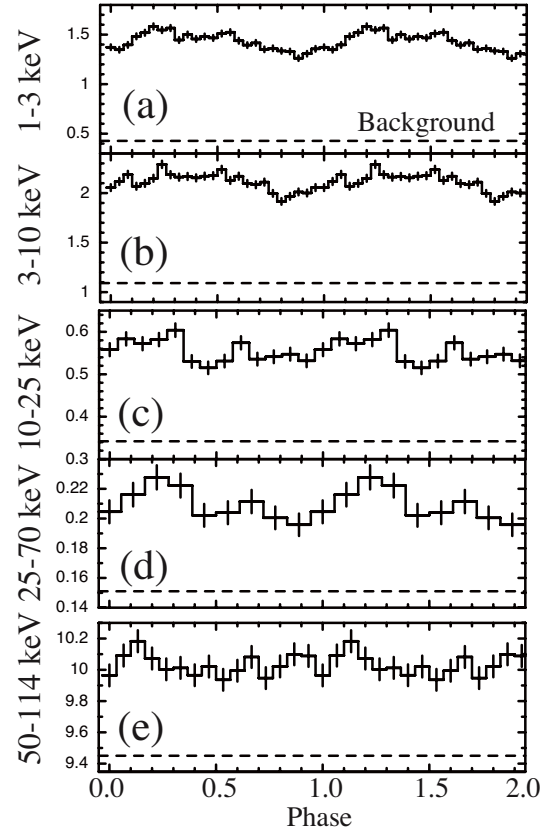


Fig. 4. Energy-sorted pulse profiles, folded at the period of equation 1. Two pulse cycles are displayed for clarify, and the background level is indicated as dashed lines. Panels (a) and (b) are extracted from XIS0 (timing mode) in the 1–3 and 3–10 keV energy ranges, respectively, while panels (c) and (d) are from HXD-PIN in the 15–30 and 30–70 keV energy ranges, respectively. Panel (e) is from the 50–114 keV GSO data. The significance of the pulsation is given in the text.

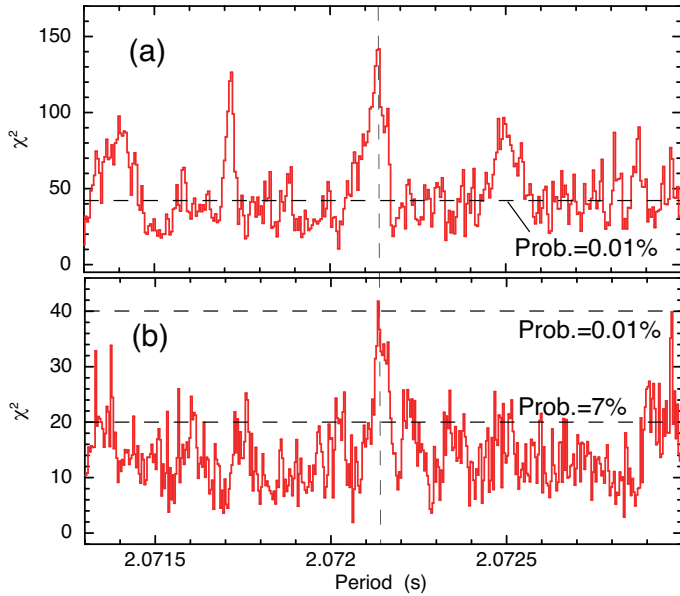


Fig. 3. Periodograms derived with an epoch-folding analysis from the 2–10 keV XIS0 P-sum mode data (panel a) and the background-inclusive 12–70 keV HXD-PIN data (panel b). The number of phase bins per period is indicated by 13 and 15 for the XIS and HXD-PIN, respectively. Typical chance probabilities are horizontal lines. Sub-peaks at 2.0717 s and 2.0725 s in panel a correspond to beats with half the spacecraft orbital period (~ 45 min).

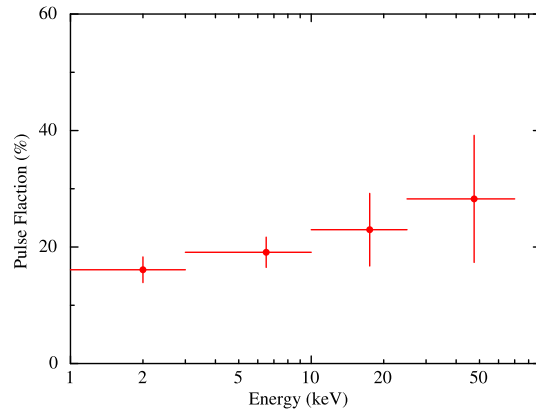


Fig. 5. The pulsed fraction shown as a function of energy.

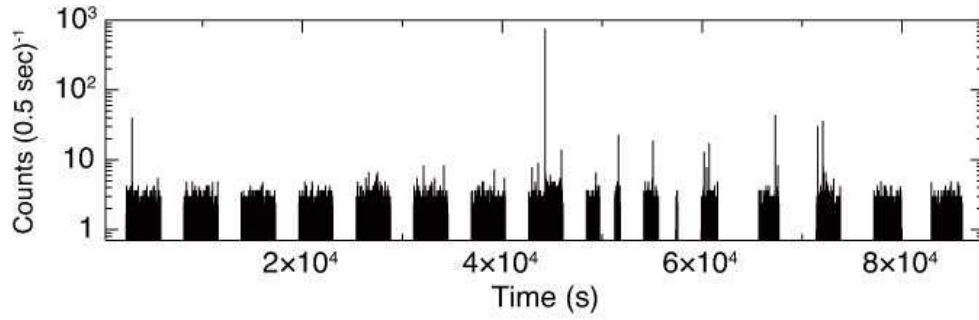


Fig. 2. A 2.0-s (with the artificial 1.5-s dead times) binned 2–10 keV light curve of the entire observation, obtained by XIS1 and XIS3, shown after background subtraction.

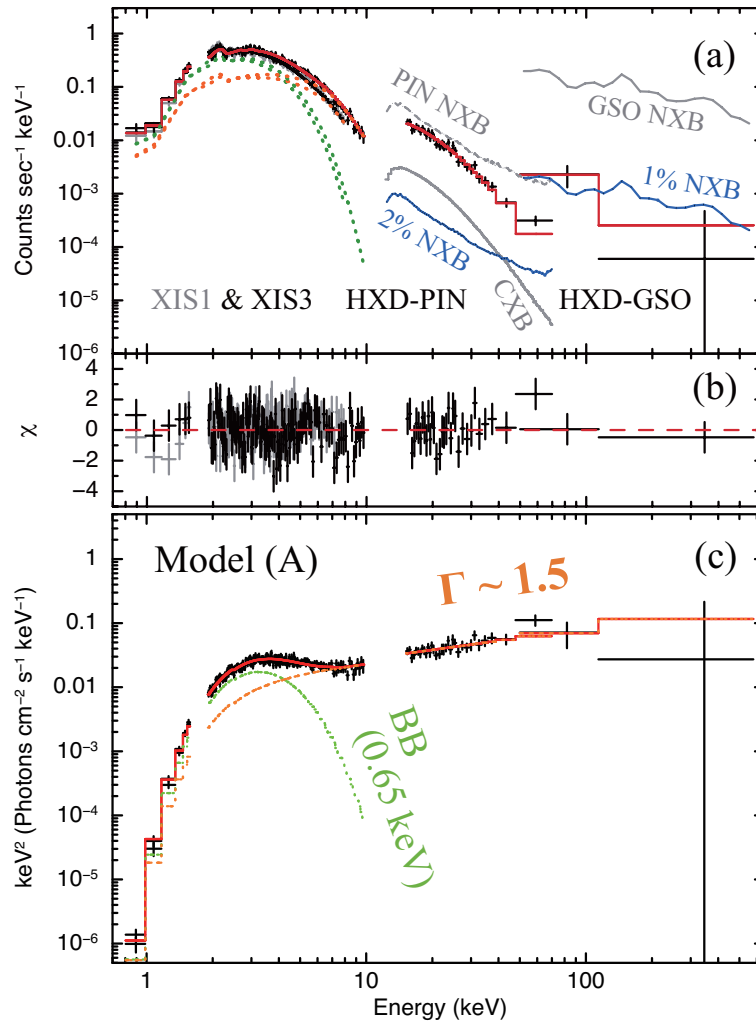


Fig. 6. (a) Persistent phase-averaged X-ray spectra of 1E 1547.0–5408, fitted simultaneously with a model consisting of a blackbody (green) and a hard power-law (red). Related background spectra are also shown. (b) Fit residuals. (c) An νF_ν form of panel (a) using Model (A).

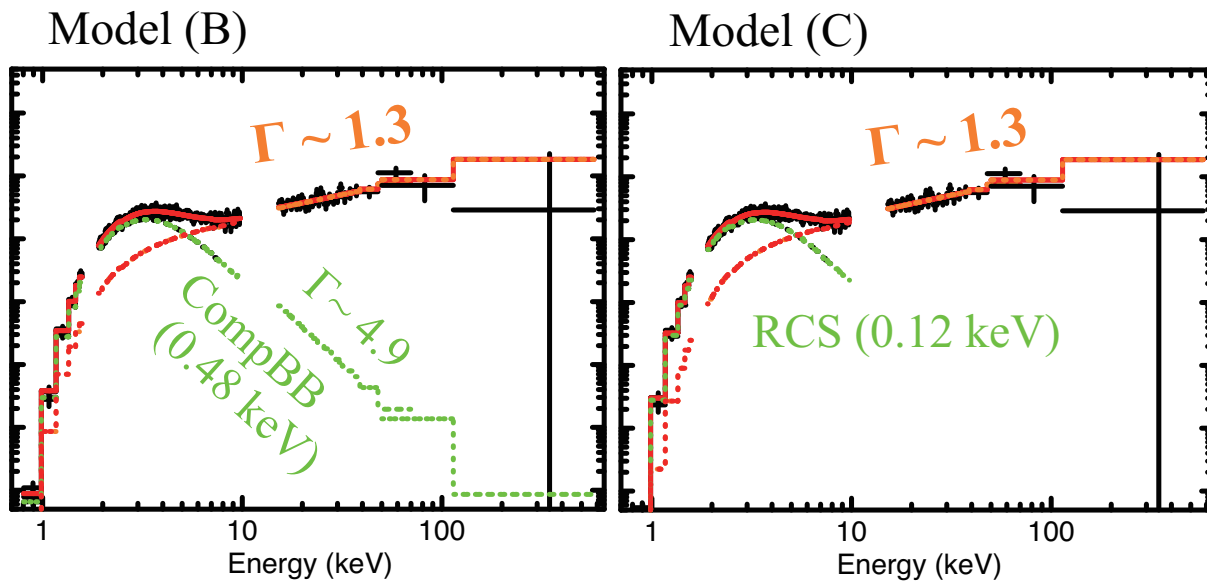


Fig. 7. The same as figure 6c, but using Model B (left) and Model C (right).